Environmental Science and Pollution Research (2021) 28:11650–11664
https://doi.org/10.1007/s11356-020-11390-y

RESEARCH ARTICLE

Construction of Ag_2O-modified g-C_3N_4 photocatalyst for rapid visible light degradation of ofloxacin

Huifen Yin [1] · Hanlu Shi [1] · Lei Sun [1,2] · Dongsheng Xia [1,2] · Xiangjuan Yuan [1,2]

Received: 12 June 2020 / Accepted: 22 October 2020 / Published online: 30 October 2020
© Springer-Verlag GmbH Germany, part of Springer Nature 2020

Abstract

The design of stable and highly efficient photocatalysts had emerged as an economic and promising way for eliminating harmful pharmaceutical pollutants. In this study, a series of Ag_2O-modified g-C_3N_4 composites with different Ag_2O amounts (denoted as Ag_2O-CN_x) were fabricated via a facile reflux condensation methodology. Ofloxacin (OFL) was chosen as a model pollutant to evaluate the degradation efficiency of the photocatalytic system. The optimal photocatalytic activity was achieved with Ag_2O-$CN_{1.0}$, which reached up to 99.1% removal of OFL after 15-min reaction and the pseudo-first-order constant was 0.469 min^{-1}, approximately 42 times higher than that of g-C_3N_4. Considering the complexity of the actual environment, the important influential factors such as catalyst dosage, initial OFL concentration, solution pH, and natural organic matter on the OFL degradation were systematically investigated. Additionally, Ag_2O-$CN_{1.0}$ showed good stability and recyclability in multiple cycle experiments. The feasible photodegradation mechanism of OFL was proposed with radical scavenger experiments, and the degradation products were determined. Furthermore, the enhanced photocatalytic activity could be ascribed to not only the high photogenerated charge separation efficiency and the surface plasmon resonance effect of metallic Ag, but also the p-n heterojunction formed between Ag_2O and g-C_3N_4. Therefore, Ag_2O-$CN_{1.0}$ was a treatment material possessing great application prospects for eliminating OFL in wastewater.

Keywords Ag_2O · g-C_3N_4 · Photocatalysis · Heterojunction · Ofloxacin · Mechanism

Introduction

Ofloxacin (OFL), one of the representative second generation of fluoroquinolone drug, is widely used for respiratory and bacterial infections in humans and animals because of its board-spectrum activity against bacteria (Lv et al. 2020; Zhang et al. 2020a). In recent years, OFL at ng L^{-1} to μg L^{-1} has been extensively detected in the aquatic environment such as wastewater, surface water, groundwater, and even drinking water (Zhu et al. 2016a; Kaur et al. 2018a). Due to the presence of hydrolysis resistance of quinolone ring, its persistence against biological degradation could pose potential risks to the safety of the aquatic ecosystem and human (Shabani et al. 2018; Adhikari et al. 2020). Thus, searching an environmentally friendly and efficient treatment method to eliminate the OFL in aqueous medium is highly desirable.

Photocatalysis, with the traits of environment friendliness, ease of performance, high efficiency, low operational cost, and sustainable energy, has received considerable attentions on the various aspects including environmental remediation, hydrogen evolution, oxygen reduction, organic pollutants removal, and carbon dioxide conversion (Kumar et al. 2018; Chang et al. 2019; Feng et al. 2020). Among tremendous photocatalysts, graphitic carbon nitride (g-C_3N_4) has been widely utilized because of its non-toxic nature, high physicochemical stability, appropriate band gap, and excellent electrical conductivity (Prabavathia et al. 2019; Shi et al. 2019; Zhang et al. 2019). Despite its towering merits, the low visible

Responsible Editor: Santiago V. Luis

Supplementary Information The online version contains supplementary material available at https://doi.org/10.1007/s11356-020-11390-y.

✉ Dongsheng Xia
dongsheng_xia@wtu.edu.cn

✉ Xiangjuan Yuan
yuanxiangjuan1986@outlook.com

[1] School of Environmental Engineering, Wuhan Textile University, Wuhan 430073, China

[2] Engineering Research Center for Clean Production of Textile Dyeing and Printing, Ministry of Education, Wuhan 430073, China

light response and fast charge recombination existing in g-C_3N_4 could be further improved to promote its practical application with enhanced photocatalytic performance.

To overcome aforementioned drawbacks, the modification of g-C_3N_4 with noble metal has been proved to be a promising strategy to improve visible light absorption and charge carrier separation due to the surface plasmon resonance (SPR) effect (Ma et al. 2016). A p-type semiconductor silver oxide (Ag_2O) with a narrow energy band gap of 1.2 eV possesses high quantum yield and strong photo-oxidative ability (Chen et al. 2015; Liu et al. 2015), which has attracted widespread concern recently. Wu et al. (2015) reported that Ag_2O-modified g-C_3N_4 exhibited the efficient property on hydrogen evolution utilizing visible light, which was about 274 times higher than that of g-C_3N_4. Chen et al. (2017a) prepared a binary photocatalyst composed of Ag_2O and g-C_3N_4 by a chemical precipitation method, presenting excellent photocatalytic degradation of dyes (i.e., methylene blue and methyl orange) in comparison to g-C_3N_4. Nevertheless, no reports have been focused on the preparation of Ag_2O-CN photocatalysts by a reflux condensation method. This reflux method is a clean, green, safe, and relatively low-temperature process, which is beneficial for the synthesis of crystalline materials with high purity and low aggregation (Mageshwari et al. 2015). Besides, the photocatalytic process and mechanism for OFL degradation in the Vis/Ag_2O-CN system have seldom been investigated.

Herein, the binary Ag_2O-CN_x photocatalysts were obtained via a reflux condensation method. The compositions, structures, and morphologies of Ag_2O-CN photocatalysts were characterized using a range of techniques. A series of operational parameters affecting the OFL degradation were comprehensively investigated. In addition, the reactive species involving OFL degradation were identified by radical scavenger experiments and electron spin resonance (ESR) technique. Finally, the possible degradation pathways and mechanism for OFL during Vis/Ag_2O-CN_x process had been proposed.

Experimental

Materials

OFL (> 98%) was obtained from TCI Chemicals (Japan). Other chemicals such as melamine, silver sulfate (Ag_2SO_4), sodium hydroxide (NaOH), hydrochloric acid (HCl), *tert*-butanol (TBA), potassium dichromate ($K_2Cr_2O_7$), *p*-benzoquinone (BQ), diammonium oxalate monohydrate (AO), and *iso*-Propyl alcohol (IPA) were received from Sinopharm Chemical Reagent Company (China). Phosphoric acid, 5, 5-dimethyl-1-pyrroline N-oxide (DMPO > 97%), 2,2,6,6-tetramethyl-4-piperidinol (TEMP), and 3, 4-dihydro-2-methyl-1 (BMPO > 97%) were purchased from Sigma-Aldrich (USA). HPLC-grade acetonitrile was supplied by Fisher Scientific (Belgium). All the reagents used in this study were at least analytical grade and without any purification. The ultrapure water obtained via the Milli-Q purification system (A10, Millipore, USA) was utilized throughout the whole experiments.

Preparation of Ag_2O-CN photocatalysts

The g-C_3N_4 was fabricated by two-step thermal treatment of melamine according to Chen et al. (2017b). To prepare Ag_2O-CN photocatalysts, 0.3 g of obtained g-C_3N_4 powder was dispersed into the ultrapure water and sonicated for 30 min at room temperature. After adding dropwise10 mL NaOH solution (0.5 M), the suspension was continuously stirred by a magnetic stirrer for 1 h. After that, different amounts of Ag_2SO_4 (0.04, 0.10, 0.20, 0.38, and 0.81 g) were introduced to the reaction system, then the suspension was refluxed at 96 °C for 2 h. Finally, the formed sample was centrifuged, washed, and dried at 60 °C for 24 h. The synthesized composites with different mass ratio of Ag_2O to g-C_3N_4 were denoted as Ag_2O-$CN_{0.1}$, Ag_2O-$CN_{0.25}$, Ag_2O-$CN_{0.5}$, Ag_2O-$CN_{1.0}$, and Ag_2O-$CN_{2.0}$, respectively.

Characterization

The Brunauer-Emmett-Teller (BET) surface area and pore size were determined by nitrogen physisorption using a Micromeritics ASAP 2010 porosimeter (USA). The crystal structure was investigated by PANalytical X'Pert Pro MPD X-ray diffractometer (XRD, Netherlands) employing Cu Kα radiation (λ = 0.154178 nm). The scanning electron microscopy (SEM) was performed on Hitachi S-4800, Japan. The transmission electron microscopy (TEM) images, the energy-dispersive X-ray spectroscopy (EDX), and elemental mapping images were obtained by JEOL JEM-2100F microscope (FEI, Japan) equipped with selected area electron diffraction (SAED). Thermogravimetric analysis (TGA) was performed by TGA55 (Netzsch, Germany) with a heat flow of 10 °C min^{-1} under nitrogen atmosphere. X-ray photoelectron spectroscopy (XPS) was conducted on VG Multilab2000 spectrometer (Thermo Fisher, USA) to analyze the chemical valence state. The UV-vis diffuse reflectance spectra (DRS) were analyzed by a PERSEE TU-1950 spectrometer (Japan) with a reference of $BaSO_4$. The photoluminescence (PL) spectra were studied by Jasco FP-6300 (Japan) at the excitation wavelength of 325 nm. The signals of active species were tested by the A300 ESR instrument (Bruker, Germany). The pH at zero point charge (PZC) of Ag_2O-$CN_{1.0}$ was determined by a drift method using a zeta potential analyzer (SurPASS 3, Anton Paar, Austria) (Zhu et al. 2015). Photoelectrochemical measurements including transient photocurrent response, electrochemical impedance spectra (EIS), and Mott-Schottky

curve were characterized on an electrochemical workstation (CS, Wuhan CorrTest, China) with a conventional three electrode system (Akhundi and Habibi-Yangjeh 2016).

Photocatalytic experiments

The activities of as-prepared photocatalysts were evaluated by the degradation of OFL. A Xe lamp (PLS-SXE300, PerfectLight, China) with a 400-nm cut-off filter was used as the light source, which was vertically placed 5 cm above the reactor during the photocatalytic reaction. The light spectrum of the Xe lamp was displayed in Fig S1. The experimental light intensity was equal to 90.52 mW cm^{-2} measured by a light meter (LI-250A, LI-COR, USA). Typically, 50 mg photocatalyst powder was dispersed in 100 mL OFL solution (10 mg L^{-1}). Before irradiation, the reaction solution was adjusted to the proper pH value with NaOH or HCl solution and stirred for 30 min in the dark to achieve the absorption-desorption equilibrium. At certain time intervals, 2 mL suspension was collected, centrifuged, and filtered.

Analytical method

The concentration of OFL was detected by a high-performance liquid chromatography (HPLC, e2695, Waters, USA) equipped with a UV-Vis detector and a C18 column (150 mm × 4.6 mm, 5 μm) maintained at 30 °C. The injection volume was 25 μL and the wavelength of the detector was 294 nm. The mobile phase consisted of 70% acetonitrile and 30% water containing 0.02% phosphoric acid with a flow rate of 1.0 mL min^{-1}. The typical HPLC chromatograms of OFL degradation during photocatalytic process were shown in Fig. S2.

The transformation products of OFL was determined by ultra-performance liquid chromatography-tandem quadrupole time-of-flight mass spectrometry (UPLC-Q-TOF-MS, AcQuity LC, Xevo G2 QTOF MS, Waters, USA) coupled to an Acquity BEH C18 column (2.1 mm × 100 mm, 1.7 μm). The injection volume was 10 μL and the column temperature was maintained at 30 °C. The mobile phases were 0.1% formic acid (solution A) and acetonitrile (solution B) at a flow rate of 0.3 mL min^{-1}. The gradient program was as follows: 0–2 min: 95%A, 5%B; 2–4 min: 40%A, 60%B; 4–6 min, 30%A, 70%B; 6–7 min: 95%A, 5%B. Mass spectral analysis was conducted in positive mode electrospray ionization (+ESI) over a mass range of 40–445 m/z. And further chromatography conditions were as follows: capillary voltage 3.0 kV, cone voltage 30 V, source temperature 100 °C, desolvation temperature 280 °C, cone gas flow rate 50 L h^{-1}, desolvation gas flow rate 500 L h^{-1}. The results identified by UPLC-Q-TOF-MS were depicted in Fig. S3, Fig. S4, and Table S1.

Results and discussion

Characterization of Ag_2O-CN_x photocatalysts

The BET surface area, pore volume, and pore size of all as-prepared photocatalysts are showed in Table 1. It is evident that the BET surface area and pore volume were gradually decreased from 44.7475 m^2 g^{-1} and 0.0701 cm^3 g^{-1} (g-C_3N_4) to 9.5527 m^2 g^{-1} and 0.0190 cm^3 g^{-1} (Ag_2O-$CN_{2.0}$), respectively, with the increase of Ag_2O loading amount. This phenomenon was probably due to the introduction of Ag_2O with a relatively low specific surface area and the blocking of the pores. Meanwhile, the N_2 adsorption/desorption isotherms of g-C_3N_4 and Ag_2O-$CN_{1.0}$ are displayed in Fig. 1a. It could be found that both g-C_3N_4 and Ag_2O-$CN_{1.0}$ showed typical type IV curve with a hysteresis loop according to the IUPAC classification (Gou et al. 2017) implying the existence of a mesoporous structure. The Barrett-Joyner-Halenda pore size distribution illustrated that the main pore size distribution of g-C_3N_4 and Ag_2O-$CN_{1.0}$ both ranged from 2 to 20 nm. The results revealed that with the augment of Ag_2O loading amount, the mesoporosity of Ag_2O-CN_x photocatalysts was apparently decreased. The Ag_2O could be anchored on the surface of g-C_3N_4 and some mesopores may be obstructed by their particles.

The thermal properties and stabilities of g-C_3N_4 and Ag_2O-$CN_{1.0}$ were evaluated by TGA in the range of 25−800 °C and the responding results are showed in Fig. 1b. It can be found that there is no significant weight loss at the temperature up to about 450 °C, indicating the outstanding thermal stability of g-C_3N_4. With the temperature further increasing, the weight lost rapidly and g-C_3N_4 completely decomposed at approximately 700 °C. For Ag_2O-$CN_{1.0}$, the slight weight loss approximately 9.1% was occurred between 150 and 480 °C, which can be ascribed to the Ag_2O decomposition. Then, the weight decreased dramatically in the temperature ranging from 480 to 700 °C, which was attributed to the rapid burning of g-C_3N_4. The residual weight about 39.1% of Ag_2O-

Table 1 The BET specific surface areas, pore volumes, and pore sizes of g-C_3N_4 and Ag_2O-CN_x composites

Catalysts	BET surface area (m^2 g^{-1})	Pore volume (cm^3 g^{-1})	Pore size (Å)
g-C_3N_4	44.7475	0.0701	62.6970
Ag_2O-$CN_{0.1}$	36.8106	0.0681	74.0833
Ag_2O-$CN_{0.25}$	35.8682	0.0653	72.8510
Ag_2O-$CN_{0.5}$	21.0588	0.0395	75.1214
Ag_2O-$CN_{1.0}$	18.6474	0.0333	71.6050
Ag_2O-$CN_{2.0}$	9.5527	0.0190	79.7319

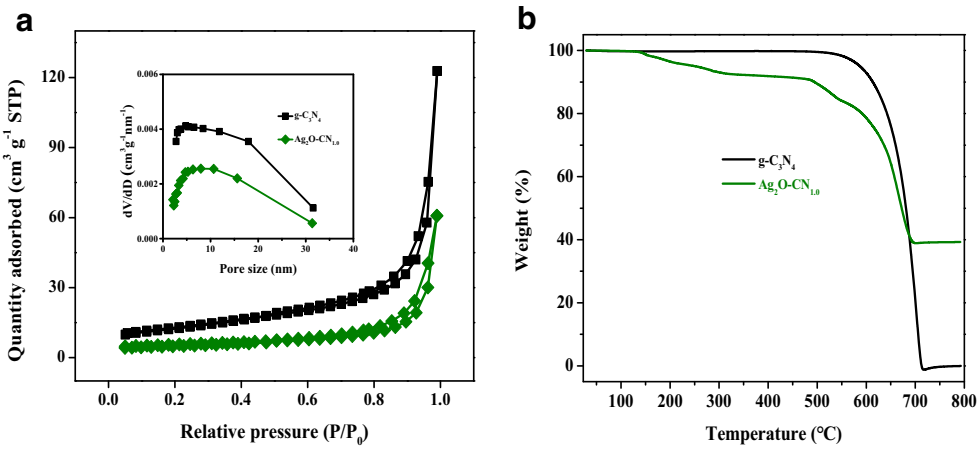

Fig. 1 **a** N_2 adsorption-desorption isotherms (insert: pore size distribution) and **b** TGA curves of g-C_3N_4 and Ag_2O-$CN_{1.0}$ composites

$CN_{1.0}$ further verified the existence of Ag_2O in the synthetic binary photocatalyst.

XRD analysis was used to investigate the phase, crystallite structure, and crystal perfection of g-C_3N_4 and Ag_2O-CN_x photocatalysts. As depicted in Fig. 2, two peaks at 12.8° and 27.5° corresponding to graphitic materials as the (100) and (002) planes could be clearly observed in g-C_3N_4, which were attributed to in-planar structural packing and inter-planar stacking signal of the aromatic system (Liu et al. 2019). The diffraction peaks of pure Ag_2O at 33.24°, 38.50°, 55.50°, and 65.87° could be assigned to the (111), (200), (220), and (311) planes of cubic structure (JCPDF#75-1532) (Hu et al. 2015). For Ag_2O-CN_x composites, no clear characteristic peaks of Ag_2O were found with low mass ratios of Ag_2O at 0.1 and 0.25, which was probably ascribe to the low content, small size, and high dispersion of Ag_2O in the composites (Xu et al. 2019), while with the increment of the Ag_2O loading amount from 0.5 to 2.0, the diffraction peak intensity of Ag_2O was notably increased. Furthermore, no diffraction peaks of metallic Ag and other impurities were detected in Ag_2O-CN_x photocatalysts, suggesting that the g-C_3N_4 and cubic Ag_2O of high purity were obtained and coexisted.

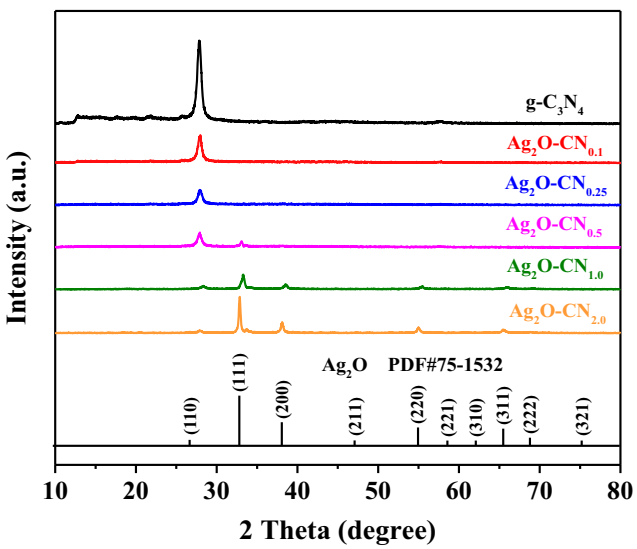

Fig. 2 XRD patterns of the g-C_3N_4 and Ag_2O-CN_x composites

The SEM images of Ag_2O-CN_x photocatalysts are showed in Fig. 3. It can be observed that all composites with different quantities of Ag_2O exhibited similar morphologies. Ag_2O-$CN_{0.1}$ (Fig. 3a) and Ag_2O-$CN_{0.25}$ (Fig. 3b) showed stacking layers appearance with no distinct Ag_2O particles. With the addition of Ag_2O contents from 0.5 to 2.0 (Fig. 3c–e), the formation of the round Ag_2O particle was observed; meanwhile, Ag_2O nanoparticles showed distinct aggregation in Ag_2O-$CN_{2.0}$. The above results were well matched with the finding of XRD patterns of Ag_2O-CN_x composites. In addition, the EDX analysis of Ag_2O-$CN_{1.0}$ in Fig. 3f demonstrated the existence of C, N, O, and Ag with an atom content of 65.07%, 15.76%, 15.59%, and 3.58%, respectively.

The morphology of g-C_3N_4 and Ag_2O-$CN_{1.0}$ were further characterized by TEM analysis. As can be seen from Fig. 4a, there were large amounts of irregular plates stacking in g-C_3N_4, revealing the laminated structure of pristine g-C3N4. For Ag_2O-$CN_{1.0}$, Ag_2O particles with average diameter about of 10 nm were uniformly distributed on g-C_3N_4 surface (Fig. 4b). The lattice spacing of Ag_2O was evaluated to be 0.27 nm corresponding to the (111) crystal planes of Ag_2O (Fig. 4c). Due to g-C_3N_4 possessed low crystallinity and weak two-dimensional ordering, its lattice spacing was difficult to observe (Li et al. 2014). Additionally, the SAED pattern of Ag_2O-$CN_{1.0}$ is showed in Fig. 4d, where a set of diffraction rings were captured suggesting the exposure of different crystal facets of Ag_2O. Moreover, elemental mapping analysis of the C, N, O, and Ag elements confirmed that Ag_2O particles were finely dispersed onto the g-C_3N_4 surface (Fig. 4e, f).

XPS was employed to confirm the chemical composition and status of Ag_2O-$CN_{1.0}$ photocatalyst. The full-scale spectrum verified the presence of Ag, O, C, and N in Ag_2O-$CN_{1.0}$ (Fig. 5a). For Ag 3d (Fig. 5b), two individual peaks with the binding energy of 368.1 eV and 374.2 eV were corresponding to Ag^+ $3d_{5/2}$ and $3d_{3/2}$ (Zhao et al. 2015). This result suggested no existence of metal Ag in Ag_2O-$CN_{1.0}$, which was in

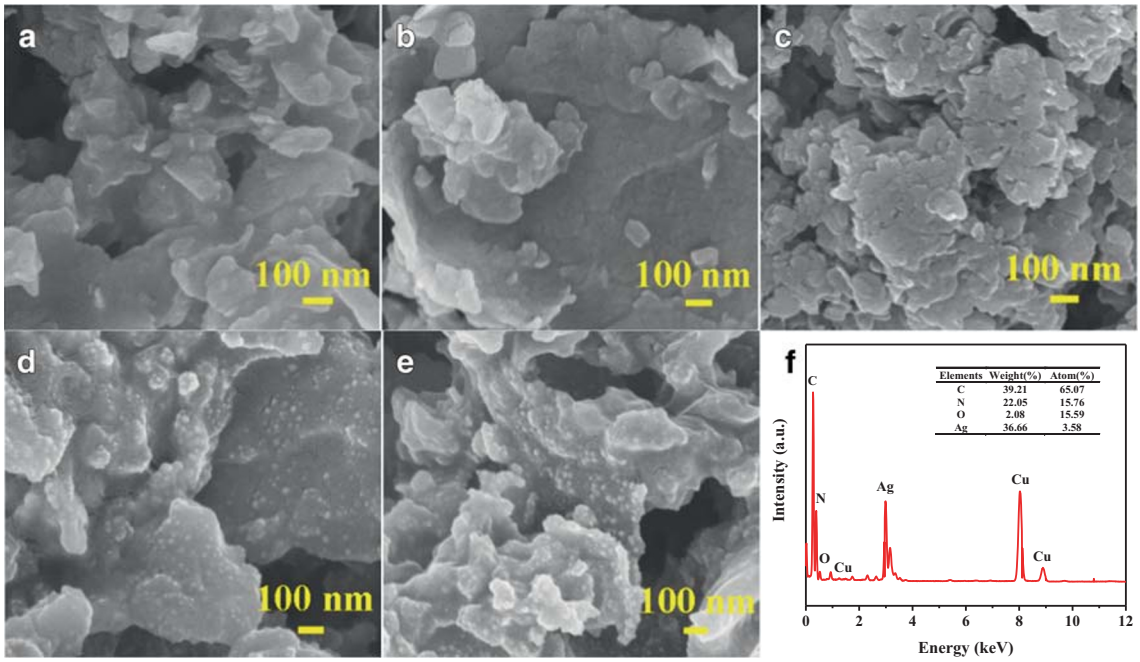

Fig. 3 SEM images of **a** Ag_2O-$CN_{0.1}$, **b** Ag_2O-$CN_{0.25}$, **c** Ag_2O-$CN_{0.5}$, **d** Ag_2O-$CN_{1.0}$, **e** Ag_2O-$CN_{2.0}$, **f** EDX spectra of Ag_2O-$CN_{1.0}$

agreement with the XRD analysis. In the case of high-resolution O 1s spectrum (Fig. 5c), two different peaks were found at 533.3 eV and 531.6 eV. The former was due to the lattice oxygen atoms in the Ag_2O (Ran et al. 2016), while the other originated from the chemisorbed oxygen of surface hydroxyl (Yu et al. 2015). The C 1s spectra (Fig. 5d) were split into three separated peaks at 288.3 eV, 286.1 eV, and 284.7 eV owing to combination of C−N groups in g-C_3N_4, sp^2-bonded in striazine rings (N−C=N) (Shang et al. 2017), the adventitious contamination and sp^2-hybridized carbon atoms in the composites (Bao and Chen 2016), respectively. Meanwhile, typical N 1s spectrum (Fig. 5e) exhibited the predominant characteristic peaks at 400.8 eV, and 398.6 eV belonged to graphitic-N and pyridinic-N (Miao et al. 2017).

UV-vis DRS was carried out to investigate the optical properties of as-prepared samples and the results are depicted in Fig. 6. Compared with pristine g-C_3N_4, Ag_2O-CN_x photocatalysts exhibited an obvious enhancement in visible light absorption edge and intensity. The band gap could be calculated according to Kubelka-Munk function: $ah\nu = k\,(h\nu\text{-}Eg)^{1/n}$, where a was the absorption coefficient, $h\nu$ was photon energy, k was a constant, n was determined by the band gap kind of a semiconductor. In this study, n was 2 owing to the direct band gaps of g-C_3N_4 (Wei and Wang 2016). In addition, the band gaps of g-C_3N_4, Ag_2O-$CN_{0.1}$, Ag_2O-$CN_{0.25}$, Ag_2O-$CN_{0.5}$, Ag_2O-$CN_{1.0}$, and Ag_2O-$CN_{2.0}$ were evaluated as 2.86 eV, 2.68 eV, 2.57 eV, 2.43 eV, 2.35 eV, and 1.96 eV, respectively. Generally, a narrower band gap was favorable for visible light absorption, which indicated that the incorporation of Ag_2O increased the utilization of low-energy photons and played a significant role in enhancement of photocatalytic performance (Wei et al. 2019).

Photocatalytic activity of Ag_2O-CN_x photocatalysts

The activities of as-prepared composites were evaluated by the OFL degradation under visible light. Before irradiation, the reaction system would reach adsorption equilibrium in dark condition within 30 min (Fig. S5). As showed in Fig. 7, only 14.6% of OFL could be removed in the presence of g-C_3N_4 with visible light. After the modification of Ag_2O, the adsorption abilities and the photocatalytic activities of Ag_2O-CN_x photocatalysts were prominently enhanced. The highest efficiency was achieved by Ag_2O-$CN_{1.0}$, and the removal rate of OFL could reach to 99.1% under visible light irradiation within 5 min. When the weight content of Ag_2O increased over 1.0, the photocatalytic performance obviously decreased. It may be attributed to excess Ag_2O particles could lead to the agglomeration, thus restricting fast separation of photogenerated charge carriers. Therefore, Ag_2O-$CN_{1.0}$ was regarded as the optimal photocatalyst for subsequent experiments.

For comparison, the degradation data of as-prepared sample in this study and other photocatalysts reported in the literature is tabulated in Table 2. The table depicted different types of catalysts prepared by different methods for OFL degradation. The advantage of the present study was that the synthetic method of Ag_2O-$CN_{1.0}$ was simple and economical. In addition, Ag_2O-$CN_{1.0}$ exhibited good performance for the degradation of OFL at the shortest irradiation time (15 min). This

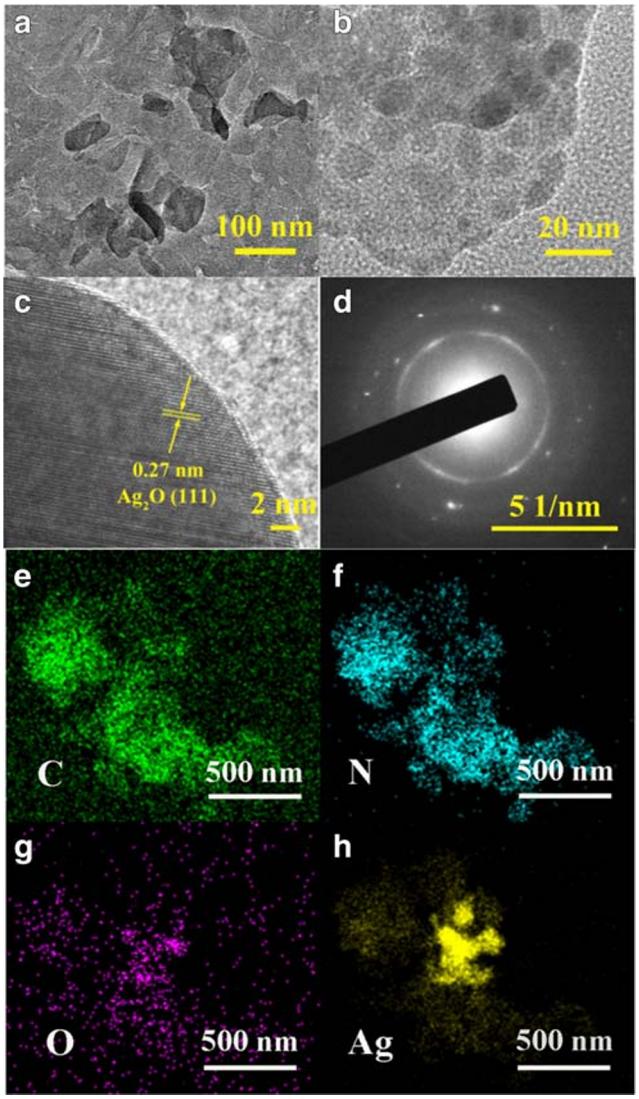

Fig. 4 TEM images of **a** g-C_3N_4, **b**, **c** Ag_2O-$CN_{1.0}$, **d** the selected area electron pattern (SAED) of Ag_2O-$CN_{1.0}$, and (**e**–**h**) elemental mapping of C, N, O, and Ag, respectively

suggested that OFL could be effectively removed using the Ag_2O-$CN_{1.0}$ composite.

It is well known that the catalyst dosage possessed a significant effect on the photocatalytic activity. Figure 8a shows the effect of Ag_2O-$CN_{1.0}$ dosage on OFL degradation. It can be observed that the adsorption capacity of Ag_2O-$CN_{1.0}$ and the removal efficiency of OFL enhanced gradually with raising catalyst dosage, which may result from the increase in the density of active sites for OFL degradation. In addition, the k values were increased from 0.2957 to 0.9754 min^{-1} with the various loading of catalyst in the range of 125 to 1500 mg L^{-1}. This phenomenon can be attributed to the fact that the high adsorption capacity was beneficial to improve photodegradation efficiency due to the full contact between target molecules and photocatalyst (Kaur et al. 2018b).

Figure 8b displays the influence of initial OFL concentration on the degradation process. It is notable that with the initial OFL concentration varied from 5 to 25 mg L^{-1}, and the k values were 0.6878, 0.3955, 0.3430, 0.3181, and 0.2824 min^{-1}, respectively. This trend can be accounted for two points: on one hand, higher OFL concentration may lead to produce more intermediates that competed with OFL molecules, resulting in limiting the OFL degradation. On the other hand, excess OFL can assimilate the partial photon entering the OFL solution (Chen et al. 2017a). Interestingly, the rate constant was reduced from 0.6878 to 0.2824 min^{-1} with initial concentration increasing from 5 to 25 mg L^{-1}, while the degradation efficiency of OFL can still reach to 98%. The results indicated that Ag_2O-$CN_{1.0}$ possessed promising application in removal of high OFL concentration.

The solution pH was an important factor affecting the surface charge of photocatalysts and OFL ionization state (Peng et al. 2012). As depicted in Fig. 8c, the influence of solution pHs (3-10) on OFL degradation in different processes such as direct photolysis, Ag_2O-$CN_{1.0}$ adsorption, and Vis/Ag_2O-$CN_{1.0}$ was investigated. Obviously, little OFL (< 1%) could be removed by direct photodegradation under all tested solution pHs. It is well known that OFL possessed three various forms at different pH: when pH < 6.00, the OFL in the aqueous solution was present in the form of cationic (OFL+), anionic form (OFL−) was dominating at pH > 8.28, and the zwitterionic form (OFL±) was primary in the pH range of 6.00–8.28 (Crespo-Alonso et al. 2013). Furthermore, the PZC of Ag_2O-$CN_{1.0}$ was 4.5, which indicated that the surface charge of Ag_2O-$CN_{1.0}$ was negative at pH > 4.5, oppositely when the pH < 4.5. At pH = 3, the surfaces of OFL and Ag_2O-$CN_{1.0}$ were both positively charged; thus, it presented poor adsorption capacity and low photocatalytic degradation. In the case of pH 4–10, the Ag_2O-$CN_{1.0}$ photocatalyst achieved 95% OFL degradation showing excellent photocatalytic performance.

Humic acid (HA), as a vital component of natural organic matter existed in surface water, had a great effect on the OFL degradation. It can be observed from Fig. 8d that the photodegradation efficiencies of OFL were evidently inhibited at the same condition in presence of HA. The k values of OFL were decreased from 0.4690 to 0.3553 min^{-1} with the HA concentration increased from 0 to 10 mg L^{-1} (as total organic carbon TOC), while the OFL degradation rates were still 99% after 15 min. Despite HA could compete with the OFL for the active species produced in the solution (Song et al. 2017), Ag_2O-$CN_{1.0}$ could still exhibit great photocatalytic performance in the wastewater, although the k declined to 0.3803 min^{-1}.

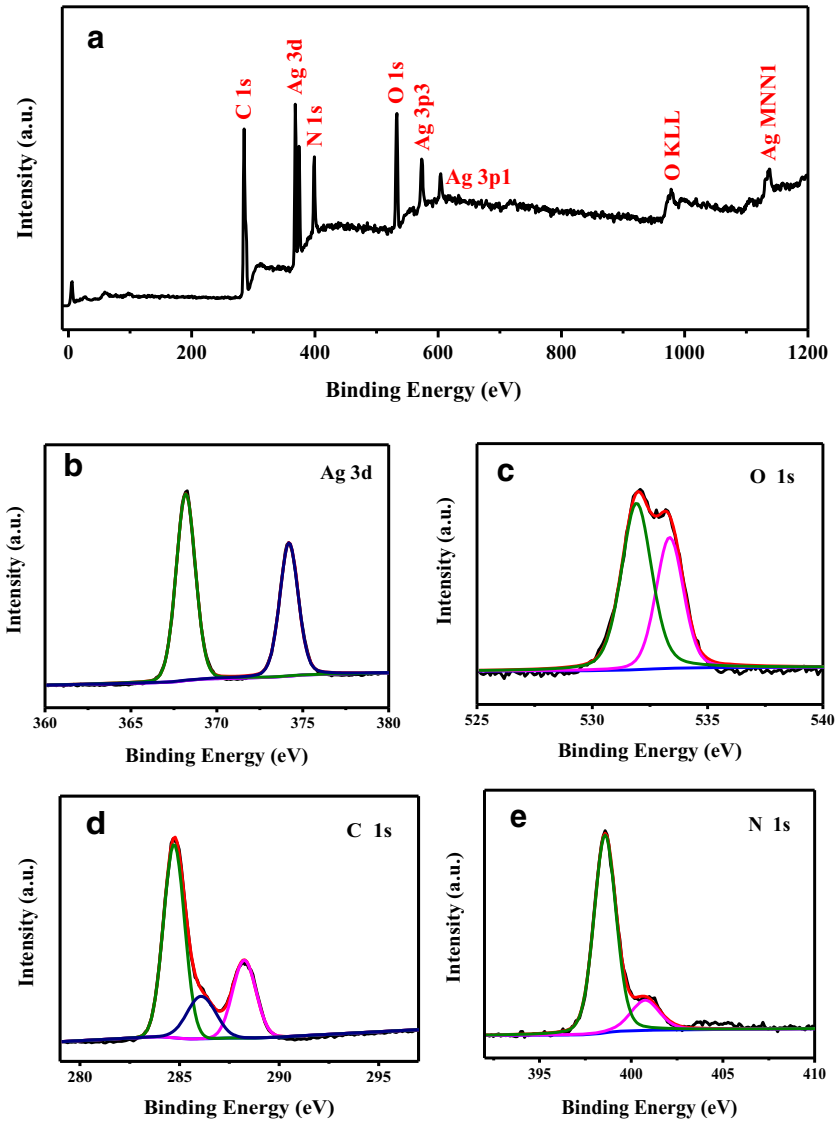

Fig. 5 XPS spectra of Ag_2O-$CN_{1.0}$ **a** survey, **b** Ag 3d, **c** O 1s, **d** C 1s, and **e** N 1s

Stability of the photocatalyst

The recycle experiments were performed to investigate the stability and recyclability of Ag_2O-$CN_{1.0}$. There was no obvious decline in OFL degradation efficiency after 5 consecutive cycles (Fig. 9a), suggesting the excellent reusability of Ag_2O-$CN_{1.0}$. In addition, the Ag^+ concentration in aqueous solution was determined less than 0.08 mg L^{-1} in each recycling experiment, which showed excellent stability and reusability. The slight leaching of Ag^+ in the solution could not weaken the catalytic activity of Ag_2O-$CN_{1.0}$ and cause secondary pollution as well. Furthermore, Fig. 9b displayed the XRD characterization results of the used and the fresh Ag_2O-$CN_{1.0}$. With the disappearance of two characteristic peaks of Ag_2O, the diffraction peaks of metallic Ag could be observed after the reaction, which demonstrated that Ag nanoparticles were produced during the photocatalytic process. From Ag 3d XPS spectrum of used Ag_2O-$CN_{1.0}$ (Fig. 9c), two new binding energy peaks at 368.6 eV and 374.8 eV could be indexed to metal Ag^0, which indicated that Ag^+ was effectively reduced to Ag^0 (He et al. 2017). The SPR effect of Ag particles could improve the utilization of visible light and facilitate the separation of photogenerated carriers (Wang et al. 2017). As showed in Fig. 9d, there was obvious reduction of Ag_2O particles on the surface of g-C_3N_4 after photodegradation.

Mechanisms of photocatalytic performance enhancement

Reactive oxidative species identification

The radical trapping experiments were conducted to identify the roles of reactive oxidative species during photocatalytic process. It is generally acknowledged that TBA and IPA were used to scavenge hydroxyl radical ($^{\bullet}OH$) formed in the solution and on the surface of the catalyst (Cai et al. 2016). The

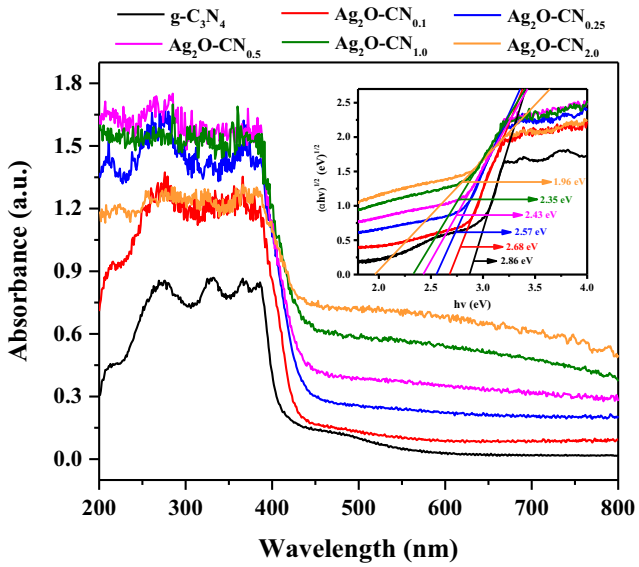

Fig. 6 UV-vis DRS spectra and of bandgap (inset) of as-synthesized composites

$K_2Cr_2O_7$, AO, NaN_3, and BQ were applied as the quenchers for electrons (e^-), holes (h^+), singlet oxygen ($^1O_2$), and superoxide radical ($^{\bullet}O_2^-$), respectively (Sun et al. 2017; Chen et al. 2019). As exhibited in Fig. 10a, the OFL degradation was almost not changed after the addition of TBA and IPA, but obviously inhibited in the presence of BQ and NaN_3 compared to the control group, which indicated that $^{\bullet}O_2^-$ and $^1O_2$ were crucial reactive species for the OFL degradation. Meanwhile, the photocatalytic activity changed slightly when $K_2Cr_2O_7$ was added, implying e^- played a minor role during the reaction process. In contrast, when AO was added, the removal efficiency of OFL was significantly decreased suggesting h^+ was also responsible for OFL degradation.

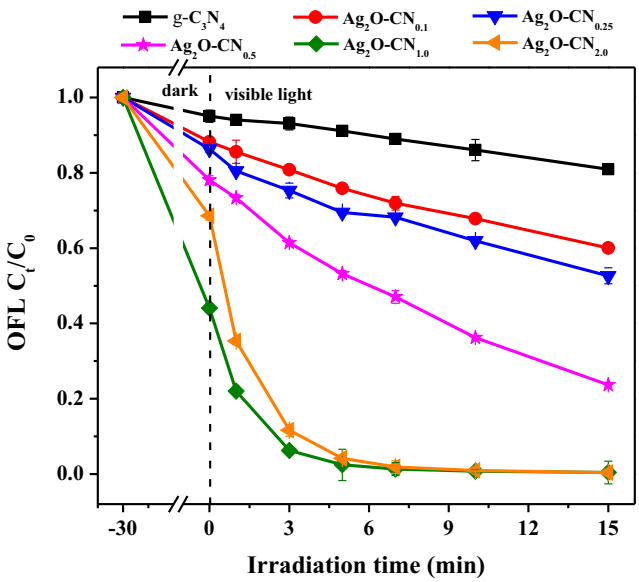

Fig. 7 Photocatalytic degradation OFL by Ag_2O-CN_x composites with various Ag_2O contents. Experimental conditions: [Ag_2O-CN_x] = 500 mg L^{-1}, $[OFL]_0$ = 10 mg L^{-1}, pH_0 = 6.0 ± 0.1, T = 293 K

Further evidence for the generation of reactive species during the photocatalytic process was derived from ESR analysis with the spin probe TEMP, DMPO, and BMPO. As seen from Fig. 10b, no obvious ESR signal could be observed in the dark. While exposed to visible light, a typical heptet of 1:2:1:2:1:2:1 for DMPO-X was observed in water solution, which might be arising from the direct oxidation of DMPO by holes (Xiong et al. 2015). In addition, the characteristic peaks for BMPO-$^{\bullet}O_2^-$ adducts were obviously observed in methanol solution with irradiation, which suggested that the $^{\bullet}O_2^-$ was generated and participated in the photocatalytic process (Ji et al. 2017). Also, a 1:1:1 triplet signal characteristic peak of TEMP-$^1O_2$ adduct was detected, which further confirmed the production of $^1O_2$ during the Vis/Ag_2O-$CN_{1.0}$ process. Based on the above results, the predominate reactive oxygen species during the OFL degradation process were $^{\bullet}O_2^-$, $^1O_2$, and h^+, which were consistent with the results of Chen et al. (2019).

Photoelectrochemical properties of Ag_2O-CN_x photocatalysts

The PL spectroscopy was an effective technology to reveal the separation rate of photogenerated carriers. In general, the low fluorescence intensity meant less recombination of e^- h^+ pairs, leading to high photocatalytic performance (Ou et al. 2018). The PL spectra of g-C_3N_4 and Ag_2O-CN_x photocatalysts are displayed in Fig. 11a. It could be found that there was a significantly diminished PL intensity in Ag_2O-CN_x composites compared with g-C_3N_4. This demonstrated that the addition of Ag_2O would depress the recombination of photogenerated carriers and facilitate the interfacial charge transfer process. It worth noting that Ag_2O-$CN_{1.0}$ showed the lowest PL intensity, indicating the best separation efficiency of the e^--h^+ pairs and highest photocatalytic activity.

The transient photocurrent response was used to reflect the migration behavior of photogenerated carriers (Zhu et al. 2016b). Figure 11b shows the photocurrent-time curves of g-C_3N_4 and Ag_2O-CN_x photocatalysts in the light switch on/off cycles. It could be clearly seen that the photocurrent densities were near zero in dark, while the photocurrent increased immediately and maintained steady values as soon as the lamp was turned on. Ag_2O-$CN_{1.0}$ displayed the highest photocurrent responses in contrast to other composites, which demonstrated the best migration ability and separation efficiency of e^--h^+ pairs. This result may be ascribed to the p-n heterojunction Ag_2O-CN photocatalyst could increase the lifetime of photogenerated carriers.

To further explore the photoelectrochemical performance of the synthesized samples, EIS analysis was performed and showed in Fig. 11c. In a Nyquist plot, smaller arc radius represented lower electron transfer resistance, indicating the

Table 2 Comparison of different photocatalysts for removing OFL in aqueous solution

Pollutants	Photocatalysts	Synthetic method	Pollutant concentration (mg L^{-1})	Removal efficiency (%)	Ref.
OFL	Co-MIL-53-NH-BT	Step-by-step assembly strategy	10	99.8% (within 120 min)	Lv et al. 2020
	UiO-67/CdS/rGO	Microwave solvothermal method	10	93.4% (within 30 min)	Zhang et al. 2020a
	$MoO_3/Ag/C_3N_4$	Hydrothermal method	20	96% (within 100 min)	Adhikari et al. 2020
	$Bi_{(X)}O_{(Y)}Cl_{(Z)}$	One-pot combustion synthesis	25	82.5% (within 180 min)	Shabani et al. 2018
	$MnWO_4$@g-C_3N_4	Ultrasonication method	10	90.4% (within 70 min)	Prabavathia et al. 2019
	Ag_2O-CN	Reflux condensation method	10	99.1% (within 15 min)	This work

faster separation efficiency at the electrode interface (Liu et al. 2016). As depicted in Fig. 11c, the size of arc radius was recognized as follows: g-C_3N_4 > Ag_2O-$CN_{0.1}$ > Ag_2O-$CN_{0.25}$ > Ag_2O-$CN_{0.5}$ > Ag_2O-$CN_{2.0}$ > Ag_2O-$CN_{1.0}$. Notably, Ag_2O-$CN_{1.0}$ possessed the smallest arc radius in all photocatalysts, suggesting superior interfacial charge transfer in accordance with the photocurrent response results. Based on the abovementioned conclusions, it can be implied that the highly enhanced photocatalyst performance of Ag_2O-$CN_{1.0}$ was not only increased visible light absorption but also improved e^--h^+ pairs separation.

The flat band potential and semiconductor types of g-C_3N_4 and Ag_2O were investigated using the Mott-Schottky tests. As showed in Fig. 11d and Fig. 11e, it is evident that flat band potentials of Ag_2O and g-C_3N_4 were about 0.72 eV and − 1.31 eV (vs. SCE) according to the x-intercept of the linear region, equivalent to − 1.07 eV and 0.96 eV (vs. NHE) (NHE = SCE+0.24 V), respectively (Wen et al. 2018). In addition, g-C_3N_4 was n-type

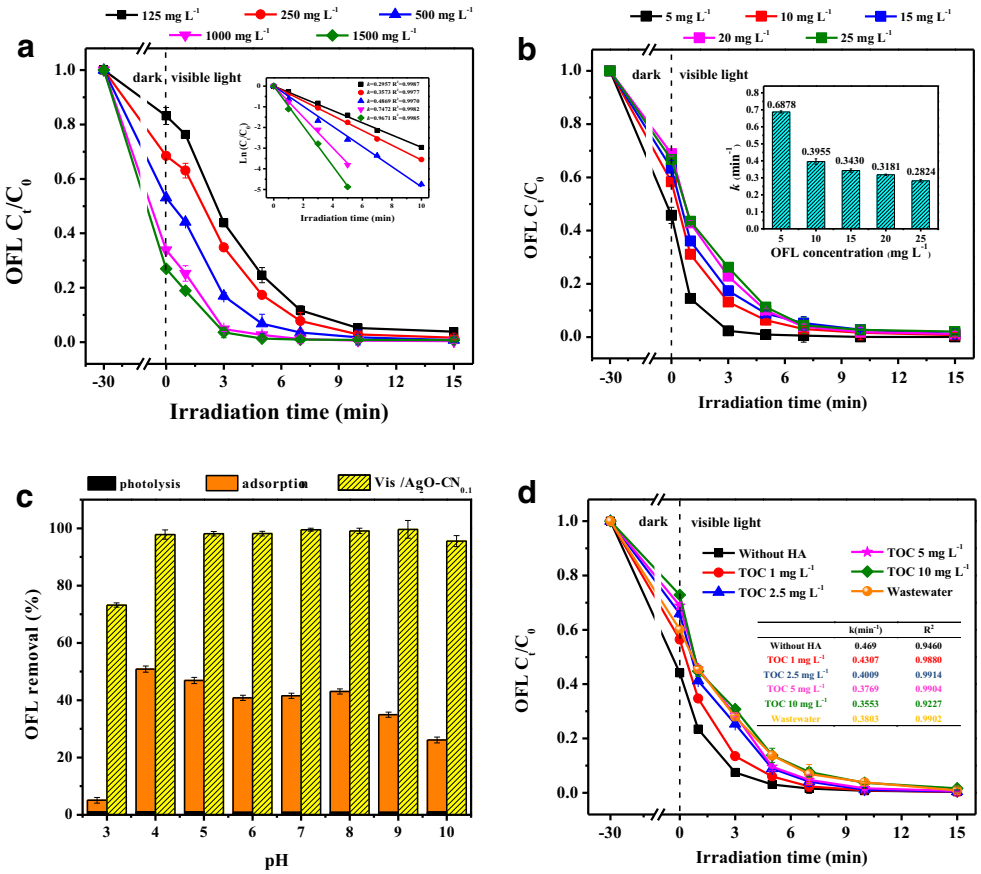

Fig. 8 The effect of **a** catalyst dose, **b** OFL concentration, **c** solution pH, **d** natural organic matter on degradation efficiency. Experimental conditions: [Ag_2O-$CN_{1.0}$] = 500 mg L^{-1} (except for **a**), $[OFL]_0$ = 10 mg L^{-1} (except for **b**), $pH_0 = 6.0 \pm 0.1$ (except for **c**), T = 293 K

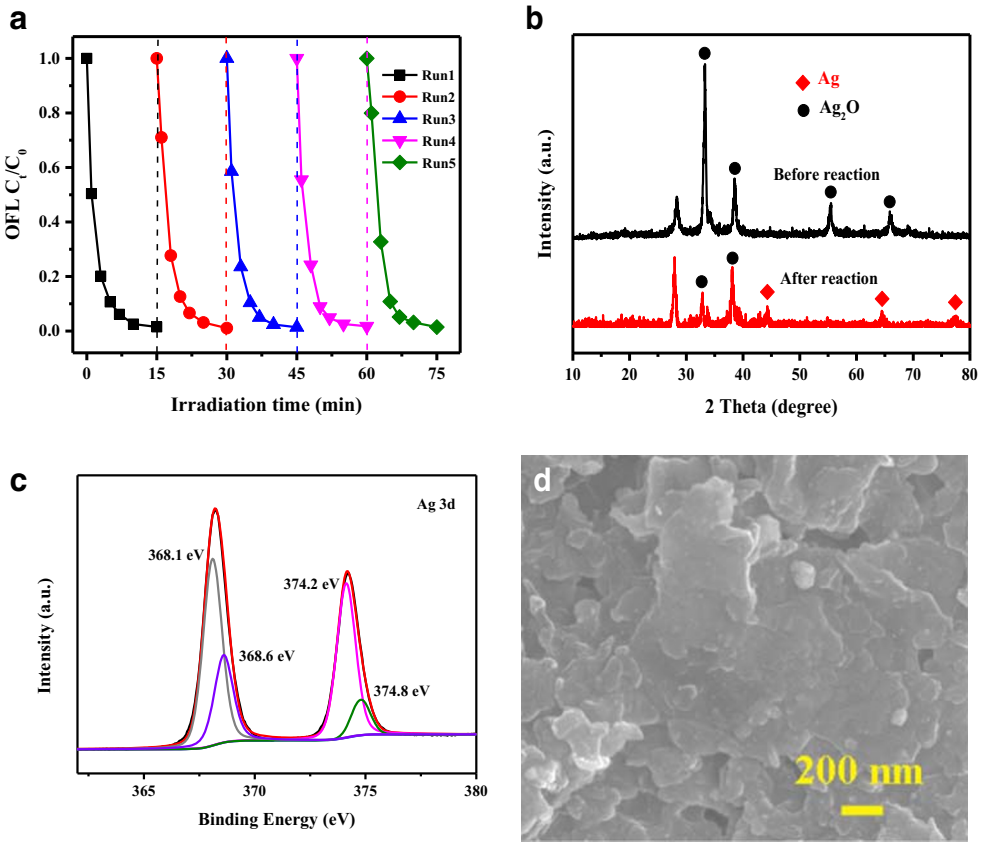

Fig. 9 **a** Recycling test of Ag_2O-$CN_{1.0}$. **b** XRD patterns, **c** Ag 3d XPS spectra, and **d** SEM image of Ag_2O-$CN_{1.0}$ after photocatalytic reaction

semiconductors (Fig. 11d) due to the positive slope in the Mott-Schottky plot. Inversely, the negative slope indicated that Ag_2O was p-type semiconductors (Fig. 11e). It can be clearly observed that an inverted "V-shape" curve in Fig. 11f demonstrating p-n heterojunction existed in Ag_2O-$CN_{1.0}$ photocatalyst.

A possible mechanism of photodegradation OFL by Ag_2O-$CN_{1.0}$ photocatalyst was proposed on account of the above experimental analysis and illustrated in Fig. 12. The CB and VB potentials of Ag_2O were calculated to be − 0.04 eV and 1.16 eV (vs. NHE) via the equation $E_{VB} = Eg + E_{CB}$ (Tian et al. 2019), and the corresponding VB and CB potentials of g-C_3N_4 were + 1.59 eV and − 1.27 eV (vs. NHE). When the Ag_2O-$CN_{1.0}$ photocatalyst was exposed to visible light, both g-C_3N_4 and Ag_2O could easily generate e^- and h^+. Considering the presence of the inner electric field in Ag_2O-$CN_{1.0}$ p-n heterojunction, the e^- had a tendency to migrate from Ag_2O to g-C_3N_4, while the transfer of h^+ was opposite (Liang et al. 2019). On the other hand, the E_{CB} of g-C_3N_4 was more negative than that of Ag_2O and the E_{VB} of Ag_2O was lower than that of g-C_3N_4, which was favorable to the migration of h^+ on the

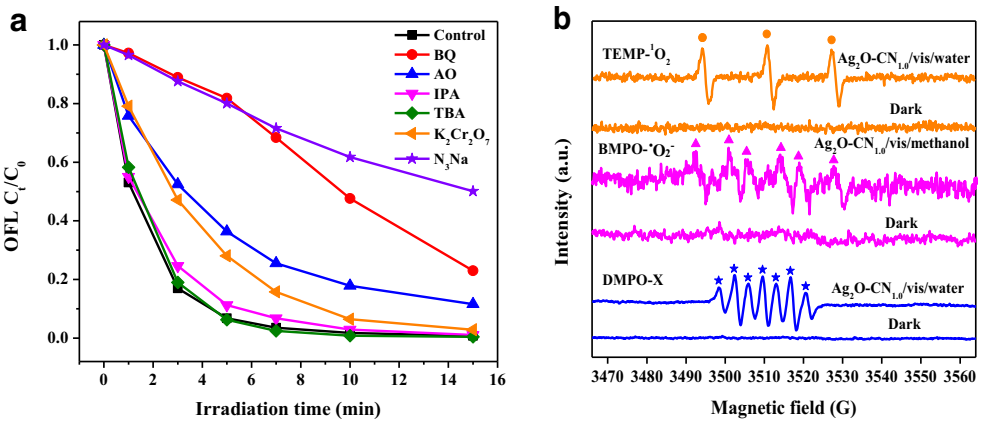

Fig. 10 **a** Effects of different scavengers on OFL degradation. **b** ESR spectra of TEMP-$^1O_2$ in aqueous solution, BMPO-$^{\bullet}O_2^-$ in methanol solution, and DMPO-X in aqueous solution. Experimental conditions: [Scavengers] = 100 mg L^{-1}, [TEMP] = 10 mM, [BMPO] = 25 mM, [DMPO] = 10 mM, [Ag_2O-$CN_{1.0}$] = 500 mg L^{-1}, $[OFL]_0$ = 10 mg L^{-1}, pH_0 = 6.0 ± 0.1, T = 293 K

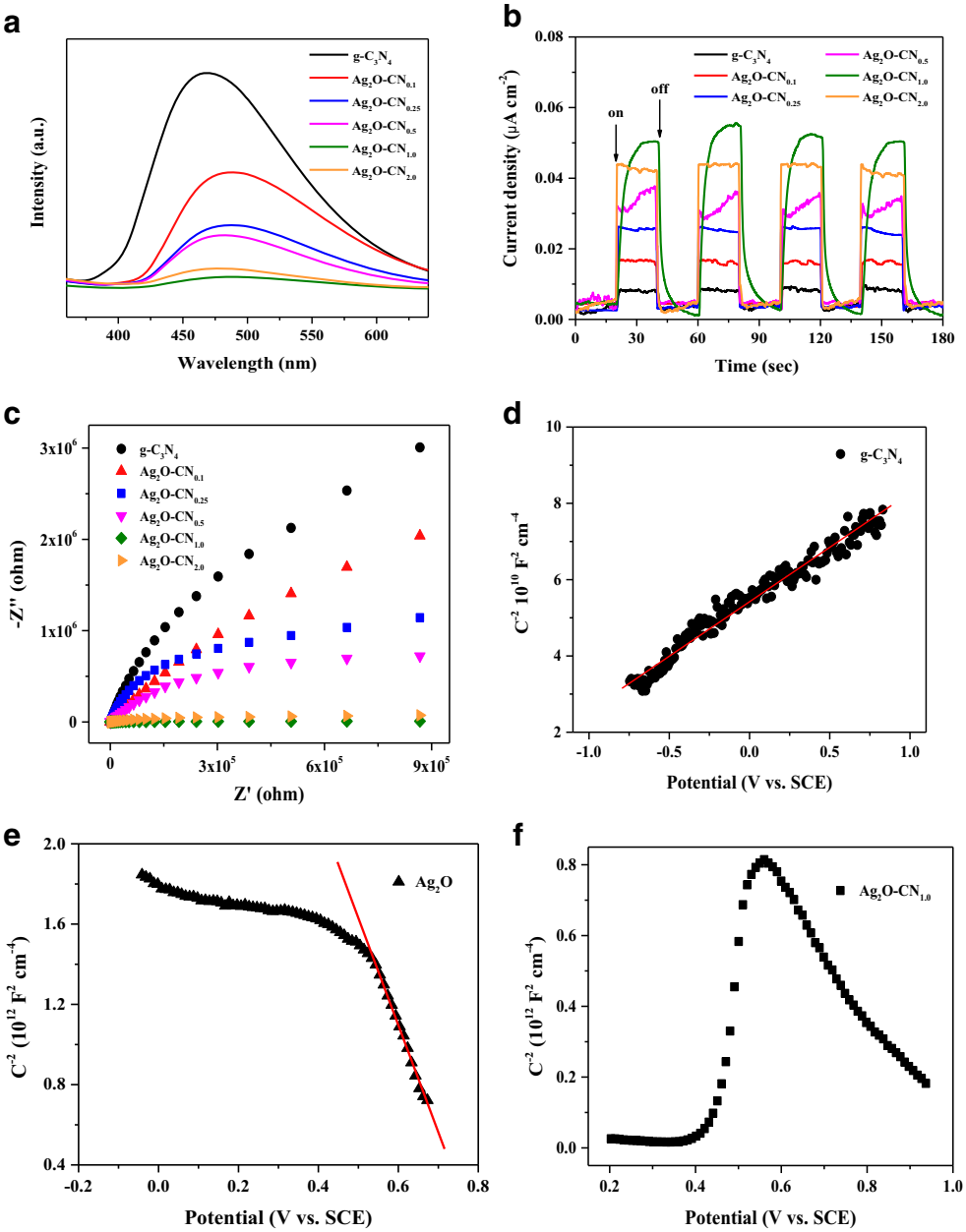

Fig. 11 PL spectra (**a**); transient photocurrent responses (**b**); electrochemical impedance spectroscopy (EIS) Nynquist plots (**c**) of the g-C_3N_4 and Ag_2O-CN_x composites. Mott-Schottky curves of **d** g-C_3N_4, **e** Ag_2O, and **f** Ag_2O-$CN_{1.0}$

VB and e^- on the CB from g-C_3N_4 to Ag_2O (Li et al. 2017). Therefore, the e^- transfer between g-C_3N_4 and Ag_2O was partially inhibited and the h^+ transfer was accelerated, which could further facilitate the separation of photogenerated charge. Meanwhile, the Ag^0 produced in the photocatalytic process worked as an electron conduction to transfer e^- to restrain the recombination of charge carriers. Furthermore, due to the E_{CB} of g-C_3N_4 was lower than $E(O_2/{}^{\bullet}O_2^-)$ (− 0.33 eV vs. NHE), the e^- on the CB of g-C_3N_4 could react with O_2 to produce ${}^{\bullet}O_2^-$ or transfer the energy to form $^1O_2$ (Shi et al. 2014). Consequently, ${}^{\bullet}O_2^-$, $^1O_2$, and h^+ had oxidation capacity to decompose the organic pollutants.

OFL degradation pathway exploration

To better elucidate the degradation mechanisms of OFL, UPLC-QTOF-MS was employed to confirm the possible intermediates in Vis/Ag_2O-$CN_{1.0}$ process. A list of the ten intermediates and MS/MS results were presented in Table S1 and Fig. S4. Based on the above results and pertinent literatures (Wammer et al. 2013; Zhu et al. 2016a; Chen et al. 2019; Zhang et al. 2020b), five main pathways of OFL degradation were proposed as depicted in Fig. 13. Firstly, the demethylation reaction occurred for OFL (m/z = 362) converting into TP1 (m/z = 348), and then TP1 was further oxidized to TP2 (m/z = 350) (Chen et al. 2019). Subsequently, TP2 was

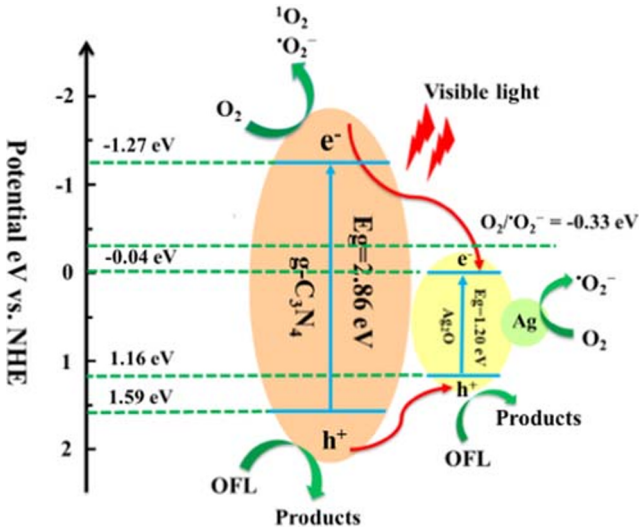

Fig. 12 Possible photocatalytic mechanism of Ag_2O-$CN_{1.0}$ composite under visible light irradiation

degraded into smaller oxygen-containing compound TP3 (m/z = 114) (Chen et al. 2019). TP4 (m/z = 279) could be formed via releasing the N-methylpiperazine (Chen et al. 2019). The generation of the TP5 (m/z = 392) was owing to the opening of piperazine ring. TP5 may further transform to TP6 (m/z = 364) via the loss of –CO group (Zhang et al. 2020a). TP7 (m/z = 378) was formed by hydroxyl group addition, and further oxidation would result in the formation of m/z 376 (Chen et al. 2019), which was not detected in our study. The TP8 with m/z = 360 was formed due to the substitution of fluorine by –OH and subsequent dealkylation of the piperazine ring to produce TP9 (m/z = 346) (Zhang et al. 2020b). Finally, these intermediates would further degrade into small molecular compounds, CO_2 and H_2O.

Conclusions

In summary, the high-efficiency Ag_2O-CN photocatalyst was successfully synthesized with spectacular photodegradation activity under visible light. Results displayed that the optimum composition mass ratio of Ag_2O and g-C_3N_4 was 1:1. Ag_2O-$CN_{1.0}$ presented the strongest oxidation ability to OFL at degradation rate of 99.1% in 15 min with a k of 0.469 min^{-1}, which was enhanced 42 times compared to g-C_3N_4. The excellent photocatalytic activity of binary photocatalysts could be ascribed to the p-n heterojunction formed after the addition of Ag_2O, which facilitated visible light utilization capacity

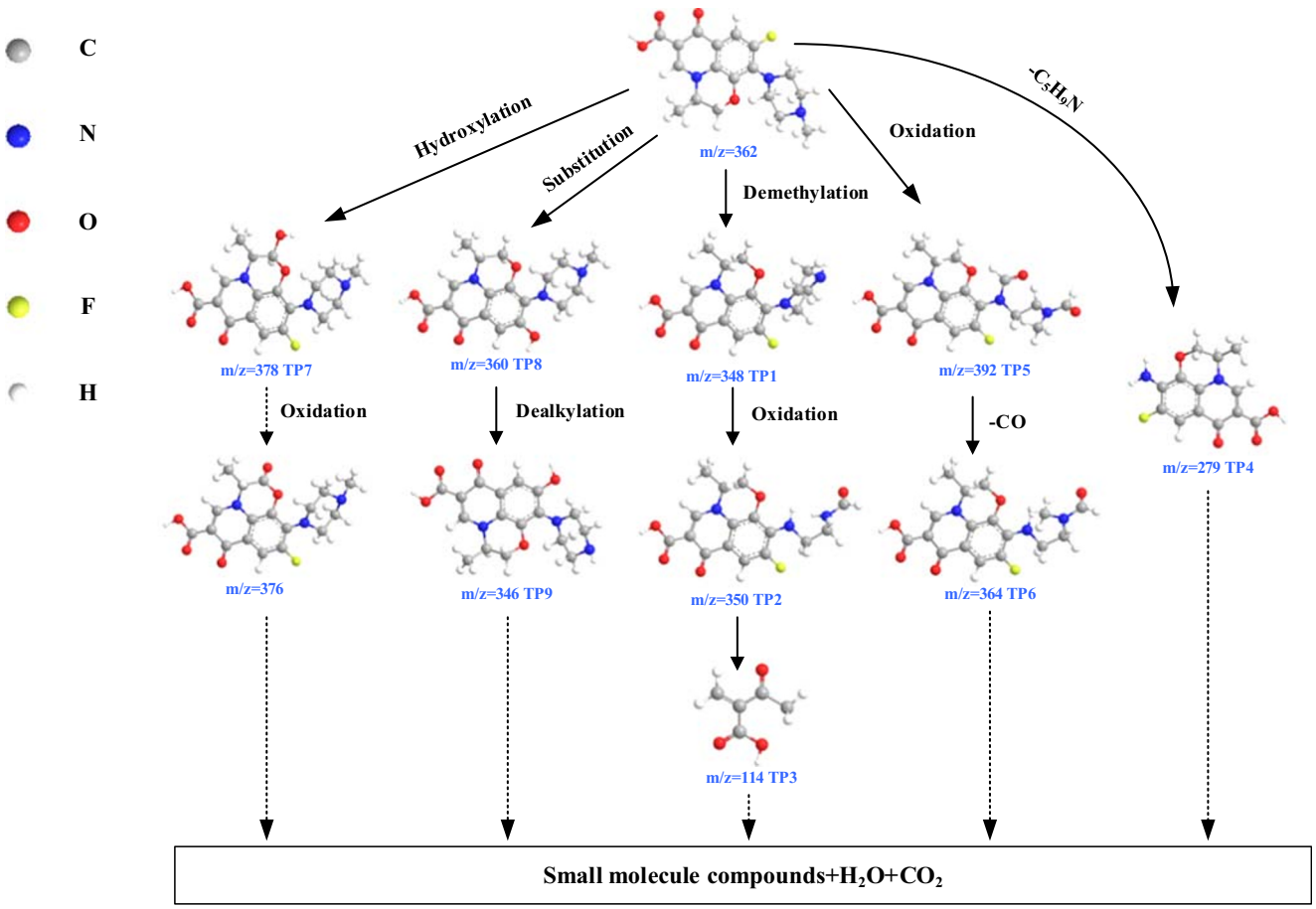

Fig. 13 Proposed degradation pathways of OFL during Vis/Ag_2O-CN process

and photogenerated charge fast transportation. In addition, the experimental results showed that the different water matrices had a slight impact on the photocatalytic activity of Ag_2O-$CN_{1.0}$. The trapping experiments and ESR technology demonstrated that $^1O_2$, $^{\bullet}O_2^-$, and h^+ were responsible for the OFL degradation. Evidences of OFL degradation pathways could be further proposed by the analysis of UPLC-Q-TOF-MS. This work demonstrated that Ag_2O-$CN_{1.0}$ had the potential to work as multifunction for degrading OFL in the aqueous environment under different conditions.

Authors' contributions Huifen Yin: methodology, investigation, writing - original draft preparation; Hanlu Shi: investigation; Lei Sun: resources; Dongsheng Xia: funding acquisition, supervision; Xiangjuan Yuan: funding acquisition, writing - review and editing, supervision.

Funding This study was funded by the National Natural Science Foundation of China (No. 51808412) and the Central Government Guidance for Local Science and Technology Development Projects for Hubei province (Nos. 2018ZYYD024, 2019ZYYD068).

Data availability All data generated or analyzed during this study are included in this published article [and its supplementary information files].

Compliance with ethical standards

Competing interests The authors declare that they have no competing interests.

Ethics approval and consent to participate Not applicable.

Consent for publication Not applicable.

References

Adhikari S, Lee HH, Kima DH (2020) Efficient visible-light induced electron-transfer in z-scheme MoO_3/Ag/C_3N_4 for excellent photocatalytic removal of antibiotics of both ofloxacin and tetracycline. Chem Eng J 391:123504. https://doi.org/10.1016/j.cej.2019.123504

Akhundi A, Habibi-Yangjeh A (2016) Novel g-C_3N_4/Ag_2SO_4 nanocomposites: fast microwave-assisted preparation and enhanced photocatalytic performance towards degradation of organic pollutants under visible light. J Colloid Interface Sci 482:165–174. https://doi.org/10.1016/j.jcis.2016.08.002

Bao YK, Chen KZ (2016) AgCl/Ag/g-C_3N_4 hybrid composites: preparation, visible light-driven photocatalytic activity and mechanism. Nano Lett 8(2):182–192. https://doi.org/10.1007/s40820-015-0076-y

Cai C, Zhang ZY, Liu J, Shan N, Zhang H (2016) Visible light-assisted heterogeneous Fenton with $ZnFe_2O_4$ for the degradation of Orange II in water. Appl Catal B Environ 182:456–468. https://doi.org/10.1016/j.apcatb.2015.09.056

Chang XM, Yao XL, Ding N, Yin XF, Zheng QM, Lu SL, Shuai DM, Sun YX (2019) Photocatalytic degradation of trihalomethanes and haloacetonitriles on graphitic carbon nitride under visible light irradiation. Sci Total Environ 682:200–207. https://doi.org/10.1016/j.scitotenv.2019.05.075

Chen L, Hua H, Yang Q, Hu CG (2015) Visible-light photocatalytic activity of Ag_2O coated Bi_2WO_6 hierarchical microspheres assembled by nanosheets. Appl Surf Sci 327:62–67. https://doi.org/10.1016/j.apsusc.2014.11.117

Chen X, Kuo DH, Hou YX (2017a) Enhancing the photodegradation of charged pollutants under visible light in Ag_2O/g-C_3N_4 catalyst by Coulombic interaction. J Mater Sci 52(9):5147–5154. https://doi.org/10.1007/s10853-017-0751-0

Chen F, Yang Q, Wang YL, Zhao JW, Wang DB, Li XM, Guo Z, Wang H, Deng YC, Niu CJ, Zen GG (2017b) Novel ternary heterojunction photcocatalyst of Ag nanoparticles and g-C_3N_4 nanosheets co-modified $BiVO_4$ for wider spectrum visible-light photocatalytic degradation of refractory pollutant. Appl Catal B Environ 205:133–147. https://doi.org/10.1016/j.apcatb.2016.12.017

Chen P, Blaney L, Cagnetta G, Huang J, Wang B, Wang YJ, Deng SB, Yu G (2019) Degradation of ofloxacin by perylene diimide supramolecular nanofiber sunlight-driven photocatalysis. Environ Sci Technol 53:1564–1575. https://doi.org/10.1021/acs.est.8b05827

Crespo-Alonso M, Nurchi VM, Biesuz R, Alberti G, Spano N, Pilo MI, Sanna G (2013) Biomass against emerging pollution in wastewater: ability of cork for the removal of ofloxacin from aqueous solutions at different pH. J Environ Chem Eng 1(4):1199–1204. https://doi.org/10.1016/j.jece.2013.09.010

Feng Z, Zeng L, Zhang QL, Ge SF, Zhao XY, Lin HJ, He YM (2020) In situ preparation of g-C_3N_4/$Bi_4O_5I_2$ complex and its elevated photoactivity in Methyl Orange degradation under visible light. J Environ Sci 87:149–162. https://doi.org/10.1016/j.jes.2019.05.032

Gou JF, Ma QL, Deng XY, Cui TQ, Zhang HX, Cheng XW, Li XL, Xie MZ, Cheng QF (2017) Fabrication of Ag_2O/TiO_2-Zeolite composite and its enhanced solar light photocatalytic performance and mechanism for degradation of norfloxacin. Chem Eng J 308:818–826. https://doi.org/10.1016/j.cej.2016.09.089

He J, Shao DW, Zheng LC, Zheng LJ, Feng DQ, Xu JP, Zhang XH, Wang WC, Wang WH, Lu F, Dong H, Cheng YH, Liu H, Zheng RK (2017) Construction of Z-scheme Cu_2O/Cu/AgBr/Ag photocatalyst with enhanced photocatalytic activity and stability under visible light. Appl Catal B Environ 203:917–926. https://doi.org/10.1016/j.apcatb.2016.10.086

Hu XX, Hu C, Wang R (2015) Enhanced solar photodegradation of toxic pollutants by long-lived electrons in Ag–Ag_2O nanocomposites. Appl Catal B Environ 176-177:637–645. https://doi.org/10.1016/j.apcatb.2015.04.040

Ji HH, Zhang LL, Hu C (2017) Chemical-bond conjugated $BiO(OH)_xI_{1-x}$-AgI heterojunction with high visible light activity and stability in degradation of pollutants. Appl Catal B Environ 218:443–451. https://doi.org/10.1016/j.apcatb.2017.06.077

Kaur A, Gupta G, Ibhadon AO, Salunke DB, Sinha ASK, Kansal SK (2018a) A Facile synthesis of silver modified ZnO nanoplates for efficient removal of ofloxacin drug in aqueous phase under solar irradiation. J Environ Chem Eng 6(3):3621–3630. https://doi.org/10.1016/j.jece.2017.05.032

Kaur M, Mehta SK, Kansal SK (2018b) Visible light driven photocatalytic degradation of ofloxacin and malachite green dye using cadmium sulphide nanoparticles. J Environ Chem Eng 6(3):3631–3639. https://doi.org/10.1016/j.jece.2017.04.006

Kumar A, Kumar A, Sharma G, Al-Muhtaseb AH, Naushad M, Ghfar AA, Stadler FJ (2018) Quaternary magnetic BiOCl/g-C_3N_4/Cu_2O/Fe_3O_4 nano-junction for visible light and solar powered degradation of sulfamethoxazole from aqueous environment. Chem Eng J 334:462–478. https://doi.org/10.1016/j.cej.2017.10.049

Li H, Liu JY, Hou WG, Du N, Zhang RJ, Tao XT (2014) Synthesis and characterization of g-C_3N_4/Bi_2MoO_6 heterojunctions with enhanced visible light photocatalytic activity. Appl Catal B Environ 160-161:89–97. https://doi.org/10.1016/j.apcatb.2014.05.019

Li YJ, Xue JY, Tian J, Song XJ, Zhang XJ, Wang XZ, Cui HZ (2017) Silver oxide decorated graphitic carbon nitride for the realization of

photocatalytic degradation over the full solar spectrum: from UV to NIR region. Sol Energy Mater Sol Cells 168:100–111. https://doi.org/10.1016/j.solmat.2017.04.031

Liang SH, Zhang DF, Pu XP, Yao XT, Han RT, Yin J, Ren XZ (2019) A novel Ag_2O/g-C_3N_4 p-n heterojunction photocatalysts with enhanced visible and near-infrared light activity. Sep Purif Technol 210:786–797. https://doi.org/10.1016/j.seppur.2018.09.008

Liu CB, Cao C, Luo XB, Luo SL (2015) Ag-bridged Ag_2O nanowire network/TiO_2 nanotube array p-n heterojunction as a highly efficient and stable visible light photocatalyst. J Hazard Mater 285:319–324. https://doi.org/10.1016/j.jhazmat.2014.12.020

Liu L, Qi YH, Lu JR, Lin SL, An WJ, Liang YH, Cui WQ (2016) A stable Ag_3PO_4 @g-C_3N_4 hybrid core@shell composite with enhanced visible light photocatalytic degradation. Appl Catal B Environ 183: 133–141. https://doi.org/10.1016/j.apcatb.2015.10.035

Liu W, Li YY, Liu FY, Jiang W, Zhang DD, Liang JL (2019) Visible-light-driven photocatalytic degradation of diclofenac by carbon quantum dots modified porous g-C_3N_4: mechanisms, degradation pathway and DFT calculation. Water Res 150:431–441. https://doi.org/10.1016/j.watres.2018.11.084

Lv SW, Liu JM, Zhao N, Li CY, Wang ZH, Wang S (2020) Benzothiadiazole functionalized Co-doped MIL-53-NH_2 with electron deficient units for enhanced photocatalytic degradation of bisphenol A and ofloxacin under visible light. J Hazard Mater 387:122011. https://doi.org/10.1016/j.jhazmat.2019.122011

Ma SL, Zhan SH, Jia YN, Shi Q, Zhou QX (2016) Enhanced disinfection application of Ag-modified g-C_3N_4 composite under visible light. Appl Catal B Environ 186:77–87. https://doi.org/10.1016/j.apcatb.2015.12.051

Mageshwari K, Sathyamoorthy R, Park J (2015) Photocatalytic activity of hierarchical CuO microspheres synthesized by facile reflux condensation method. Powder Technol 278:150–156. https://doi.org/10.1016/j.powtec.2015.03.004

Miao XL, Shen XP, Wu JJ, Jia ZY, Wang JH, Kong LR, Liu MM, Song CS (2017) Fabrication of an all solid Z-scheme photocatalyst g-C_3N_4/GO/AgBr with enhanced visible light photocatalytic activity. Appl Catal A Gen 539:104–113. https://doi.org/10.1016/j.apcata.2017.04.009

Ou M, Wan SP, Zhong Q, Zhang SL, Song Y, Guo LN, Cai W, Xu YL (2018) Hierarchical Z-scheme photocatalyst of g-C_3N_4 @Ag/$BiVO_4$ (040) with enhanced visible-light-induced photocatalytic oxidation performance. Appl Catal B Environ 221:97–107. https://doi.org/10.1016/j.apcatb.2017.09.005

Peng HB, Pan B, Wu M, Liu R, Zhang D, Wu D, Xing BS (2012) Adsorption of ofloxacin on carbon nanotubes: solubility, pH and cosolvent effects. J Hazard Mater 211-212:342–348. https://doi.org/10.1016/j.jhazmat.2011.12.063

Prabavathia SL, Saravanakumara K, Mamba G, Muthuraj V (2019) 1D/2D $MnWO_4$ nanorods anchored on g-C_3N_4 nanosheets for enhanced photocatalytic degradation ofloxacin under visible light irradiation. Colloids Surf A Physicochem Eng Asp 581:123845. https://doi.org/10.1016/j.colsurfa.2019.123845

Ran R, Meng XC, Zhang ZS (2016) Facile preparation of novel graphene oxide-modified Ag_2O/Ag_3VO_4/$AgVO_3$ composites with high photocatalytic activities under visible light irradiation. Appl Catal B Environ 196:1–15. https://doi.org/10.1016/j.apcatb.2016.05.012

Shabani M, Haghighi M, Kahforoushan D (2018) One-pot combustion fabrication of grain-like mesoporous intra-heterostructure $Bi_{(x)}O_{(y)}Cl_{(z)}$ nanophotocatalyst with substantial solar-light-driven degradation of antibiotic ofloxacin: influence of various fuels. Catal Sci Technol 8:4052–4069. https://doi.org/10.1039/c8cy00547h

Shang YY, Chen X, Liu WW, Tan PF, Chen HY, Wu LD, Ma C, Xiong X, Pan J (2017) Photocorrosion inhibition and high-efficiency photoactivity of porous g-C_3N_4/Ag_2CrO_4 composites by simple microemulsion-assisted co-precipitation method. Appl Catal B Environ 204:78–88. https://doi.org/10.1016/j.apcatb.2016.11.025

Shi L, Liang L, Ma J, Wang FX, Sun JM (2014) Enhanced photocatalytic activity over the Ag_2O–g-C_3N_4 composite under visible light. Catal Sci Technol 4(3):758. https://doi.org/10.1039/c3cy00871a

Shi HL, He R, Sun L, Cao G, Yuan XJ, Xia DS (2019) Band gap tuning of g-C_3N_4 via decoration with AgCl to expedite the photocatalytic degradation and mineralization of oxalic acid. J Environ Sci 84:1–12. https://doi.org/10.1016/j.jes.2019.04.009

Song YL, Tian JY, Gao SS, Shao PH, Qi JY, Cui FY (2017) Photodegradation of sulfonamides by g-C_3N_4 under visible light irradiation: effectiveness, mechanism and pathways. Appl Catal B Environ 210:88–96. https://doi.org/10.1016/j.apcatb.2017.03.059

Sun M, Zeng Q, Zhao X, Shao Y, Ji PG, Wang CQ, Yan T, Du B (2017) Fabrication of novel g-C_3N_4 nanocrystals decorated Ag_3PO_4 hybrids: enhanced charge separation and excellent visible-light driven photocatalytic activity. J Hazard Mater 339:9–21. https://doi.org/10.1016/j.jhazmat.2017.06.003

Tian L, Yang XF, Cui XK, Liu QQ, Tang H (2019) Fabrication of dual direct Z-scheme g-C_3N_4/MoS_2/Ag_3PO_4 photocatalyst and its oxygen evolution performance. Appl Surf Sci 463:9–17. https://doi.org/10.1016/j.apsusc.2018.08.209

Wammer KH, Korte AR, Lundeen RA, Sundberg JE, McNeill K, Arnold WA (2013) Direct photochemistry of three fluoroquinolone antibacterials: norfloxacin, ofloxacin, and enrofloxacin. Water Res 47(1): 439–448. https://doi.org/10.1016/j.watres.2012.10.025

Wang WG, Liu Y, Zhang HY, Qian YN, Guo ZC (2017) Re-investigation on reduced graphene oxide/Ag_2CO_3 composite photocatalyst: an insight into the double-edged sword role of RGO. Appl Surf Sci 396:102–109. https://doi.org/10.1016/j.apsusc.2016.11.030

Wei ZD, Wang R (2016) Hierarchical BiOBr microspheres with oxygen vacancies synthesized via reactable ionic liquids for dyes removal. Chin Chem Lett 27(5):769–772. https://doi.org/10.1016/j.cclet.2016.03.013

Wei ZD, Liu JY, Fang WJ, Xu MQ, Qin Z, Jiang Z, Shangguan WF (2019) Photocatalytic hydrogen evolution with simultaneous antibiotic wastewater degradation via the visible-light-responsive bismuth spheres-g-C_3N_4 nanohybrid: Waste to energy insight. Chem Eng J 358:944–954. https://doi.org/10.1016/j.cej.2018.10.096

Wen XJ, Niu CG, Zhang L, Liang C, Zeng GM (2018) A novel Ag_2O/CeO_2 heterojunction photocatalysts for photocatalytic degradation of enrofloxacin: possible degradation pathways, mineralization activity and an in depth mechanism insight. Appl Catal B Environ 221: 701–714. https://doi.org/10.1016/j.apcatb.2017.09.060

Wu M, Yan JM, Zhang XW, Zhao M, Jiang Q (2015) Ag_2O modified g-C_3N_4 for highly efficient photocatalytic hydrogen generation under visible light irradiation. J Mater Chem A 3(30):15710–15714. https://doi.org/10.1039/c5ta03358f

Xiong T, Dong F, Zhou Y, Fu M, Ho WK (2015) New insights into how RGO influences the photocatalytic performance of $BiOIO_3$/RGO nanocomposites under visible and UV irradiation. J Colloid Interface Sci 447:16–24. https://doi.org/10.1016/j.jcis.2015.01.068

Xu J, Gao QZ, Bai XJ, Wang ZP, Zhu YF (2019) Enhanced visible-light-induced photocatalytic degradation and disinfection activities of oxidized porous g-C_3N_4 by loading Ag nanoparticles. Catal Today 332:227–235. https://doi.org/10.1016/j.cattod.2018.07.024

Yu W, Liu XJ, Chu HP, Zhu G, Li JL, Liu JY, Niu LY, Sun Z, Pan LK (2015) Enhancement of visible light photocatalytic activity of Ag_2O/F-TiO_2 composites. J Mol Catal A Chem 407:25–31. https://doi.org/10.1016/j.molcata.2015.06.015

Zhang C, Li Y, Shuai DM, Shen Y, Xiong W, Wang L (2019) Graphitic carbon nitride (g-C_3N_4)-based photocatalysts for water disinfection and microbial control: a review. Chemosphere 214:462–479. https://doi.org/10.1016/j.chemosphere.2018.09.137

Zhang DD, Qi JJ, Ji HD, Li S, Chen L, Huang TB, Xu CK, Chen XM, Liu W (2020a) Photocatalytic degradation of ofloxacin by perovskite-

type $NaNbO_3$ nanorods modified g-C_3N_4 heterojunction under simulated solar light: theoretical calculation, ofloxacin degradation pathways and toxicity evolution. Chem Eng J 400:125918. https://doi.org/10.1016/j.cej.2020.125918

Zhang SP, Wang YM, Cao Z, Xu J, Hua J, Huang Y, Cui CZ, Liu HL, Wang HL (2020b) Simultaneous enhancements of light-harvesting and charge transfer in UiO67/CdS/rGO composites toward ofloxacin photo-degradation. Chem Eng J 381:122771. https://doi.org/10.1016/j.cej.2019.122771

Zhao W, Guo Y, Wang SM, He H, Sun C, Yang SG (2015) A novel ternary plasmonic photocatalyst: ultrathin g-C_3N_4 nanosheet hybrided by $Ag/AgVO_3$ nanoribbons with enhanced visible-light photocatalytic performance. Appl Catal B Environ 165:335–343. https://doi.org/10.1016/j.apcatb.2014.10.016

Zhu BC, Xia PF, Ho WK, Yu JG (2015) Isoelectric point and adsorption activity of porous g-C_3N_4. Appl Surf Sci 344:188–195. https://doi.org/10.1016/j.apsusc.2015.03.086

Zhu Z, Lu ZY, Wang DD, Tang X, Yan YS, Shi WD, Wang WS, Gao NL, Yao X, Dong HJ (2016a) Construction of high-dispersed Ag/Fe_3O4/g-C_3N_4 photocatalyst by selective photo-deposition and improved photocatalytic activity. Appl Catal B Environ 182:115–122. https://doi.org/10.1016/j.apcatb.2015.09.029

Zhu LY, Santiago-Schubel B, Xiao HX, Hollert H, Kueppers S (2016b) Electrochemical oxidation of fluoroquinolone antibiotics: mechanism, residual antibacterial activity and toxicity change. Water Res 102:52–62. https://doi.org/10.1016/j.watres.2016.06.005

Publisher's note Springer Nature remains neutral with regard to jurisdictional claims in published maps and institutional affiliations.